atoms

MDPI

Article

Ab Initio Quadrupole-Invariant Analysis of Neutron-Rich Deformed Nuclei Around $N = 28$

Liu-Yuan Shen [1,2], Xin-Peng Wang [1,2], Hong-Hui Li [1,2], Hong-Yu Zhu [3], Wei Zuo [1,2] and Qi Yuan [1,2,*]

[1] Institute of Modern Physics, Chinese Academy of Sciences, Lanzhou 730000, China; shenliuyuan24@mails.ucas.ac.cn (L.-Y.S.); wangxinpeng@impcas.ac.cn (X.-P.W.); lihonghui@impcas.ac.cn (H.-H.L.); zuowei@impcas.ac.cn (W.Z.)
[2] School of Nuclear Science and Technology, University of Chinese Academy of Sciences, Beijing 100049, China
[3] Flerov Laboratory of Nuclear Reactions, Joint Institute for Nuclear Research (JINR), 141980 Dubna, Russia; zhuhy@jinr.ru
* Correspondence: yuanqi@impcas.ac.cn

Abstract

We present an ab initio quadrupole-invariant study of neutron-rich nuclei around $N = 28$. Effective Hamiltonians and consistently evolved $E2$ operators are obtained from chiral NN+3N interactions using the ab initio valence-space in-medium similarity renormalization group, and the resulting $E2$ matrix elements are used to extract the deformation parameters. Along the even–even $N = 28$ isotonic chain, the β values increase systematically from ^{48}Ca to ^{40}Mg, providing a direct deformation signature of the weakening of the $N = 28$ shell closure. The extracted β and γ values show a prolate–oblate–triaxial evolution of the 0_1^+ states from ^{40}Mg to ^{42}Si and ^{44}S, while the 0_2^+ states remain mainly in the prolate-to-triaxial region. Extending the analysis to the neighboring $N = 27$ and 29 isotones, we find a systematic evolution from strongly prolate Mg isotopes, to oblate-side Si isotopes, and to prolate-to-triaxial S isotopes. These results provide a unified picture of quadrupole deformation, triaxiality, and configuration coexistence around $N = 28$.

Keywords: Ab initio calculations; deformation; quadrupole invariants

1. Introduction

Understanding how shell structure evolves far from stability is one of the central goals of modern nuclear structure physics. The traditional magic numbers, which are well established near the valley of stability [1,2], can be strongly modified in neutron-rich systems because of changes in the single-particle spectrum and the enhanced role of correlations [3–8]. Quadrupole collectivity is a particularly sensitive probe of such shell evolution: reduced low-lying excitation energies, enhanced electric-quadrupole transition strengths, and the appearance of deformed or coexisting structures all signal the weakening of spherical shell closures.

The neutron number $N = 28$ offers a particularly important example. It is robust in the doubly magic nucleus ^{48}Ca, while below calcium the rapid lowering of the 2_1^+ excitation energies, the enhancement of $E2$ transition strengths, and the appearance of low-lying coexisting structures indicate a strong reduction in the spherical shell gap [9–21]. The erosion of the gap between the neutron $\nu 0f_{7/2}$ and $\nu 1p_{3/2}$ orbitals favors quadrupole correlations, and the active proton degrees of freedom in the *sd* shell further amplify collectivity through quasi-SU(3), pseudo-SU(3), and the Jahn–Teller effect [22–28]. As a

Check for updates

Academic Editor: Giuseppe Mandaglio

Received: 16 July 2026
Revised: 10 August 2026
Accepted: 12 August 2026
Published: 12 August 2026

Copyright: © 2026 by the authors. Licensee MDPI, Basel, Switzerland. This article is an open access article distributed under the terms and conditions of the Creative Commons Attribution (CC BY) license.

consequence, the neutron-rich nuclei around $N = 28$ display a rich interplay between shell erosion, deformation, and shape coexistence.

A number of theoretical studies have investigated the neutron-rich $N = 28$ region, including shell-model (SM) calculations [22–27,29,30], beyond-mean-field (BMF) approaches [31–34], antisymmetrized molecular dynamics (AMD) calculations [28,35,36], and ab initio approaches [20,21,37]. These studies have suggested a rapid shape evolution in the even–even $N = 28$ isotones, including well-developed deformation in ^{40}Mg and ^{42}Si, shape coexistence in ^{44}S, and a prolate–oblate–prolate evolution of the ground-state-associated structures from ^{40}Mg through ^{42}Si to ^{44}S [11,14,15,28,38–40]. Furthermore, previous SM analyses based on quadrupole rotational invariants have shown that the triaxial degree of freedom plays an important role in ^{43,44}S [30]. The low-lying structures in the sulfur isotopes have been interpreted in terms of shape and configuration coexistence, including the coexistence of the $3/2^-_1$ ground state with the $7/2^-_1$ isomer in ^{43,45}S and the appearance of low-lying deformed and triaxial structures in ^{44}S [21,30]. These interpretations are also connected to the rich experimental spectroscopy of sulfur isotopes in this mass region [41–48]. AMD and BMF calculations have also emphasized triaxiality, large shape fluctuations, and competing configurations, especially in ^{44}S [28,33,34].

Recent ab initio valence-space in-medium similarity renormalization group (VS-IMSRG) calculations have provided a microscopic description of this region using consistently evolved Hamiltonians and electromagnetic operators [20,21,37]. Those studies used spectra, $B(E2)$ values, and spectroscopic quadrupole moments Q_s to identify rotational sequences and configuration-coexisting structures in neutron-rich nuclei around $N = 28$. These results showed that ab initio calculations can describe the emergence of quadrupole collectivity and provide microscopic insight into shape coexistence and isomeric structures in this mass region. However, Q_s values and transition maps by themselves do not provide a direct state-by-state representation of deformation in the β–γ plane. In particular, a small or vanishing Q_s does not necessarily imply a spherical shape; it may also reflect triaxiality, K mixing, or fluctuations between prolate and oblate components. A complementary analysis is therefore useful to convert the ab initio $E2$-transition matrix elements into quadrupole invariants. Quadrupole invariants provide such a bridge between $E2$ matrix elements and intrinsic-shape language. Following the quadrupole-sum-rule approach of Kumar and Cline [49,50], the second- and third-order quadrupole invariants allow one to extract the magnitude of quadrupole collectivity β and the triaxiality indicator γ from $E2$ matrix elements, while higher-order invariants further provide estimates of the fluctuations in these deformation parameters [30,51,52].

In this work, we perform an ab initio quadrupole-invariant analysis of neutron-rich nuclei around $N = 28$. Starting from chiral NN+3N interactions, we use the VS-IMSRG to consistently derive effective Hamiltonians and $E2$ operators, and then construct quadrupole invariants and extract deformation parameters β and γ for the low-lying states. We first examine the even–even $N = 28$ isotones from ^{48}Ca to ^{40}Mg, focusing on the evolution of the $0^+_{1,2}$ and $2^+_{1,2}$ states. We then analyze the detailed low-lying structures of ^{40}Mg, ^{42}Si, and ^{44}S by combining β, γ, Q_s, and $E2$-transition maps. Finally, we extend the analysis to the neighboring $N = 27$ and $N = 29$ Mg, Si, and S isotopes to obtain a systematic β-γ picture of shape evolution around $N = 28$.

2. Materials and Methods

2.1. Valence-Space In-Medium Similarity Renormalization Group

We start from the intrinsic A-body Hamiltonian

$$H = \sum_{i<j}\left[\frac{(\vec{p}_i - \vec{p}_j)^2}{2mA} + v_{ij}^{\mathrm{NN}}\right] + \sum_{i<j<k} v_{ijk}^{\mathrm{3N}}, \tag{1}$$

where $\vec{p}$ is the nucleon momentum, m is the nucleon mass, and v^{NN} and v^{3N} denote the NN and 3N interactions, respectively. In this work we employ the chiral NN+3N interaction EM1.8/2.0 [53–56], which is composed of a next-to-next-to-next-to-leading order NN interaction softened by the similarity renormalization group (SRG) evolution with momentum resolution scale $\lambda = 1.8$ fm^{-1} and a next-to-next-to-leading order 3N force with momentum cutoff $\Lambda = 2.0$ fm^{-1}. The calculation is performed in a harmonic-oscillator basis at $\hbar\omega = 16$ MeV with $e_{\max} = 2n + \ell = 14$ and $E_{3\,\max} = 14$. This model space was adopted in the previous VS-IMSRG calculations for neutron-rich nuclei around $N = 28$ [20,21,57], which is sufficient for convergence.

In practical calculations, Hamiltonian (1) is transformed to a Hartree–Fock basis and rewritten in normal-ordered form,

$$H = E_0 + \sum_{ij} f_{ij}\{a_i^\dagger a_j\} + \frac{1}{4}\sum_{ijkl}\Gamma_{ijkl}\{a_i^\dagger a_j^\dagger a_l a_k\}, \tag{2}$$

where the residual normal-ordered three-body term is neglected, while the dominant effects of the 3N interaction are retained through ensemble normal ordering. The VS-IMSRG aims to decouple the Hamiltonian from the large Hilbert space into a small valence space. This decoupling is achieved by solving the flow equation

$$\frac{dH(s)}{ds} = [\eta(s), H(s)], \tag{3}$$

with the anti-Hermitian generator $\eta(s)$. In the present work, the Magnus formalism is employed with all operators truncated at the two-body level [58–64],

$$H_{\mathrm{eff}} = e^{\Omega} H e^{-\Omega}, \qquad \hat{O}_{\mathrm{eff}} = e^{\Omega}\hat{O}e^{-\Omega}, \tag{4}$$

where $\hat{O}$ denotes an observable operator. In practical calculations, we take protons in the *sd* shell and neutrons in the *pf* shell above the ^{28}O core as the valence space. The effective Hamiltonians and $E2$ operators for this valence space are derived consistently by VS-IMSRG. The valence-space Hamiltonian is subsequently diagonalized with the large-scale shell-model code KSHELL [65]. $E2$ transition matrix elements calculated with the effective $E2$ operator are then used for the quadrupole-invariant analysis.

2.2. Quadrupole Invariants and Fluctuation Ranges

In the classical geometrical description, the nuclear shape is parametrized by the quadrupole deformation variables β and γ, where β specifies the overall deformation magnitude and γ describes the axial asymmetry [66]. In the usual convention, $\gamma = 0^\circ$ and 60° correspond to axially symmetric prolate and oblate shapes, respectively, while intermediate values describe triaxial shapes. In the principal-axis frame, the nonzero components of the electric quadrupole tensor are $Q_{20} = \frac{3ZeR_0^2}{4\pi}\beta\cos\gamma$, and $Q_{2\pm2} = \frac{3ZeR_0^2}{4\pi\sqrt{2}}\beta\sin\gamma$. Scalar combinations constructed from this tensor are rotationally invariant, with the second- and third-order invariants being proportional to β^2 and $\beta^3\cos(3\gamma)$, respectively. In the rigid-rotor limit, these invariants recover the conventional geometrical deformation parameters. For soft or configuration-mixed nuclei, however, they characterize moments of the deformation distribution rather than a unique static shape, while the higher-order quadrupole invariants determine the corresponding fluctuations in β and γ.

In this work, the deformation parameters are extracted from the quadrupole-invariant method of Kumar and Cline [49,50], using the large-scale shell-model implementation of ref. [52]. Higher-order rotational invariants beyond the third order can be constructed through different J couplings, where J denotes the coupling of a pair of $E2$ operators [52]. In the present work we use the $J = 0$ couplings [52]. For a state $|s\rangle$, the required scalar invariants are written as

$$\langle Q^2 \rangle = \sqrt{5}\,\langle s||[E2 \times E2]^0||s\rangle, \tag{5}$$

$$\langle Q^3 \cos(3\gamma)\rangle = -\sqrt{\frac{35}{2}}\,\langle s||[[E2 \times E2]^2 \times E2]^0||s\rangle, \tag{6}$$

$$\langle Q^4 \rangle = 5\,\langle s||[[E2 \times E2]^0 \times [E2 \times E2]^0]^0||s\rangle, \tag{7}$$

$$\langle Q^6 \cos^2(3\gamma)\rangle = \frac{35}{2}\,\langle s||[[[E2 \times E2]^2 \times E2]^0 \times [[E2 \times E2]^2 \times E2]^0]^0||s\rangle, \tag{8}$$

$$\langle Q^6 \rangle = 5\sqrt{5}\,\langle s||[[[E2 \times E2]^0 \times [E2 \times E2]^0]^0 \times [E2 \times E2]^0]^0||s\rangle. \tag{9}$$

The quantity $\langle Q^3 \rangle$ entering the definition of γ is estimated by the even-order invariants as

$$\langle Q^3 \rangle = \left[\frac{1}{2}(\langle Q^2\rangle^{1/2} + \langle Q^4\rangle^{1/4})\right]^3. \tag{10}$$

The invariant deformation parameters are defined as

$$\beta = \frac{4\pi\,\langle Q^2\rangle^{1/2}}{3ZeR_0^2}, \qquad \cos(3\gamma) = \frac{\langle Q^3 \cos(3\gamma)\rangle}{\langle Q^3\rangle}. \tag{11}$$

with $R_0 = 1.2A^{1/3}$ fm. The fluctuations of β and $\cos(3\gamma)$ are defined by the higher-order invariants as

$$\Delta\beta = \frac{\beta\sqrt{\langle Q^4\rangle - \langle Q^2\rangle^2}}{2\langle Q^2\rangle}, \qquad \Delta\cos(3\gamma) = \sqrt{\frac{\langle Q^6 \cos^2(3\gamma)\rangle}{\langle Q^6\rangle} - \left(\frac{\langle Q^3 \cos(3\gamma)\rangle}{\langle Q^3\rangle}\right)^2}. \tag{12}$$

Figure 1 shows the convergence of the quadrupole-invariant deformation parameters with respect to the number of intermediate states. For the 0_1^+ and 0_2^+ states in ^{44}S, the calculated β, $\Delta\beta$, γ, and $\Delta\gamma$ are well converged with 100 states. The deformation parameters for the other nuclei studied in this work are also calculated using 100 states, with convergence checked in the same manner.

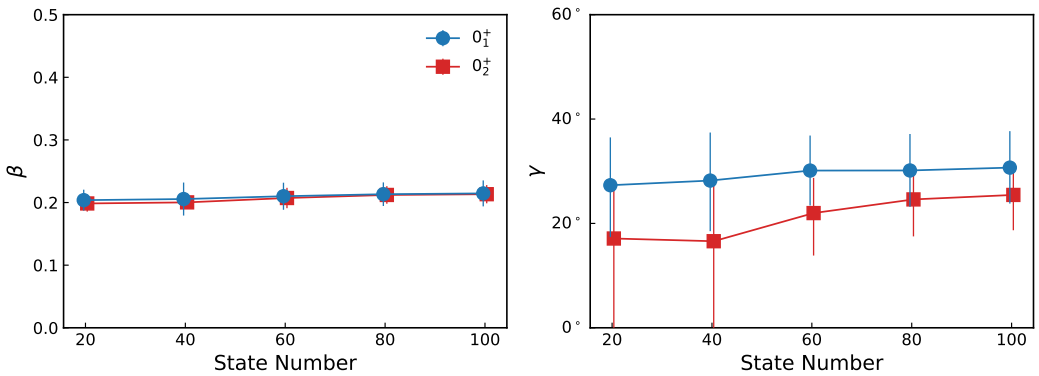

Figure 1. Convergence of the quadrupole-invariant deformation parameters for the 0_1^+ and 0_2^+ states in ^{44}S as a function of the number of intermediate states. The vertical ranges denote the corresponding fluctuation estimates.

3. Results

Extensive experimental and theoretical studies have shown that the robust $N = 28$ shell closure in ^{48}Ca is strongly eroded toward the neutron-rich Mg, Si, and S isotopes, where quadrupole collectivity and deformation emerge [4,6,20,21]. Figure 2 provides an invariant-based visualization of this evolution. From ^{48}Ca to ^{40}Mg, the β values of the $0^+_{1,2}$ states increase systematically. The very small β value of the ^{48}Ca ground state reflects its nearly spherical doubly magic character, whereas the low-lying states in ^{40}Mg reach $\beta \approx 0.30$, indicating well-developed quadrupole collectivity. This trend gives a direct deformation signature of the weakening of the $N = 28$ shell closure toward the neutron-rich region.

The low-lying spectra and $B(E2)$ strengths of ^{40}Mg, ^{42}Si, and ^{44}S, calculated using the same VS-IMSRG framework and EM1.8/2.0 interaction as in the present study, were compared in detail with the available experimental data in our previous work [20]. The low-lying spectra were reasonably reproduced, whereas the absolute $B(E2)$ strengths exhibited the systematic underestimation commonly found in VS-IMSRG calculations [67]. For example, the calculated excitation energy of the 2^+_1 state in ^{44}S, 1.39 MeV, is close to the experimental value of 1.329 MeV, whereas the calculated $B(E2; 2^+_1 \rightarrow 0^+_1) = 30\ e^2\text{fm}^4$ is below the experimental value of $44(6)\ e^2\text{fm}^4$ [68]. Consequently, the absolute β values extracted here may also be underestimated. In contrast, γ is determined from ratios of quadrupole invariants and is therefore expected to be less sensitive to an approximately common rescaling of the $E2$ matrix elements. Nevertheless, nonuniform truncation effects among different matrix elements cannot be excluded, and their quantitative impact on the extracted β and γ values requires further investigation.

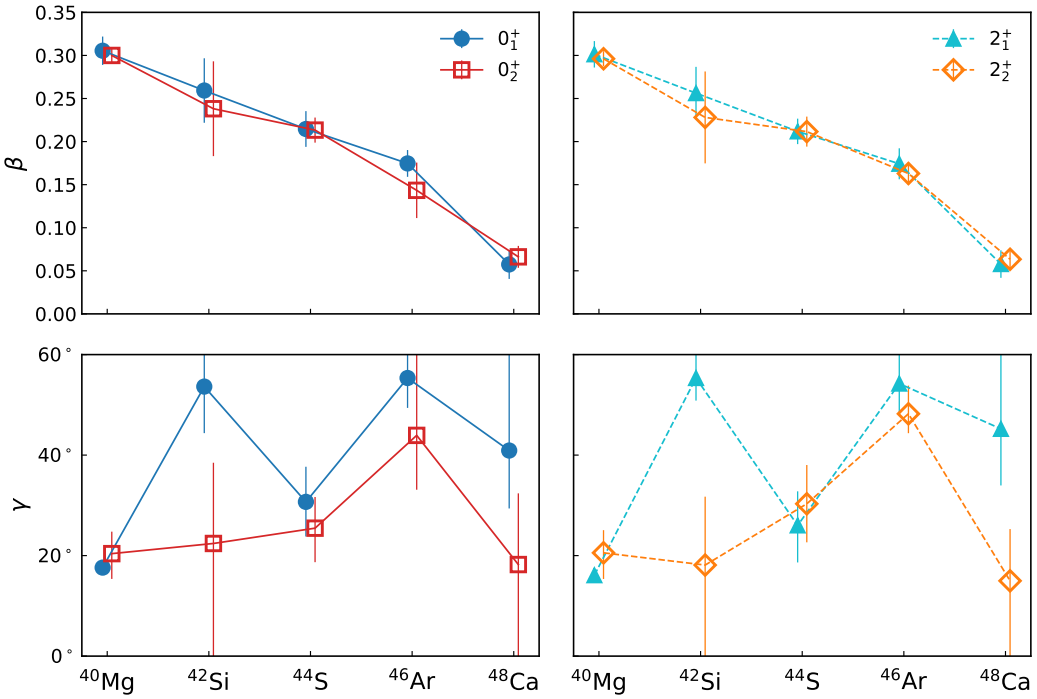

Figure 2. Calculated β and γ of the low-lying $0^+_{1,2}$ and $2^+_{1,2}$ states along the $N = 28$ isotonic chain.

Beyond the overall deformation magnitude, the evolution of γ reveals a pronounced state dependence of the low-lying quadrupole structures. In the usual axial-rotor convention, the sign change of $Q_s(2^+_1)$ from negative in ^{40}Mg, to positive in ^{42}Si, and back to negative in ^{44}S suggests a prolate–oblate–prolate evolution of the ground-state-associated structures, as shown in Table 1. The invariant-derived β and γ values refine this picture.

For ^{40}Mg, the 0_1^+ state is characterized by a relatively small γ, indicating a prolate deformation. In contrast, the 0_1^+ state of ^{42}Si moves toward the oblate deformation, while the 0_1^+ state of ^{44}S lies close to $\gamma \approx 30^\circ$, suggesting a more non-axial or triaxial character. The 0_2^+ states exhibit a similar β trend to the 0_1^+ states, with increasing quadrupole collectivity from ^{48}Ca toward ^{40}Mg. Their γ evolution, however, is not identical to that of the ground states. In ^{40}Mg, ^{42}Si, and ^{44}S, the γ values of the 0_2^+ states mostly lie in the 0°–30° region, corresponding to prolate or triaxial deformation. In contrast, the AMD results suggest that the 0_1^+ state of ^{40}Mg is prolate, while the 0_2^+ state is oblate [28].

In ^{42}Si, the 0_1^+ and 0_2^+ states have comparable β values but clearly different γ values. This indicates that the two 0^+ states represent competing quadrupole structures with comparable collectivity and distinct triaxiality. In particular, the large γ-fluctuation range of the 0_2^+ state in ^{42}Si indicates a broad distribution in the triaxial degree of freedom, suggesting a γ-soft character. However, the AMD results suggest that the 0_2^+ state of ^{42}Si is mainly distributed in the small-β spherical region [28]. Furthermore, our calculations show that the β and γ values of the 2_1^+ and 2_2^+ states in these nuclei closely follow those of the 0_1^+ and 0_2^+ states, respectively, supporting the interpretation of the 0_1^+–2_1^+ and 0_2^+–2_2^+ pairs as two correlated low-lying quadrupole structures.

It is also instructive to compare our results with the simple SU(3) description of the *sd*-shell valence protons. Assuming an $N = 28$ neutron shell closure, the ground-state bands of ^{40}Mg, ^{42}Si, and ^{44}S are expected to be described by the highest-weight SU(3) irreducible representations $(4,2)$, $(6,0)$, and $(2,4)$, respectively, while the first excited $K = 0^+$ bands, starting from the 0_2^+ states, are associated with the next-highest-weight irreducible representations $(0,4)$, $(0,6)$, and $(4,0)$, respectively [69–72]. This simple picture is qualitatively consistent with our results for the prolate-side ground state of ^{40}Mg and the prolate-side 0_2^+ state of ^{44}S. For ^{42}Si, it also predicts comparable deformation magnitudes but distinct shapes for the two 0^+ states, although their prolate–oblate ordering differs from our calculations. These differences may arise from the erosion of the $N = 28$ shell closure and correlations beyond this simplified proton-only SU(3) description.

Table 1. Calculated excitation energies E_x, spectroscopic quadrupole moments Q_s, and deformation parameters β and γ for ^{40}Mg, ^{42}Si, and ^{44}S.

^{40}Mg	0_1^+	0_2^+	2_1^+	2_2^+	4_1^+	4_2^+
E_x (MeV)	0.00	1.48	0.68	1.99	1.92	3.16
Q_s (e fm^2)	-	-	-12.0	9.6	-15.5	19.4
β	0.31(2)	0.30(1)	0.30(2)	0.30(1)	0.29(2)	0.28(1)
$\gamma(^\circ)$	18^{+1}_{-1}	20^{+4}_{-5}	16^{+1}_{-1}	21^{+5}_{-5}	14^{+2}_{-2}	14^{+4}_{-6}
^{42}Si	0_1^+	0_2^+	2_1^+	2_2^+	4_1^+	4_2^+
E_x (MeV)	0.00	2.82	0.81	3.45	2.35	4.25
Q_s (e fm^2)	-	-	13.2	-10.2	16.6	11.1
β	0.26(4)	0.24(6)	0.26(3)	0.23(5)	0.25(2)	0.20(3)
$\gamma(^\circ)$	54^{+6}_{-9}	22^{+16}_{-22}	55^{+5}_{-4}	18^{+14}_{-18}	56^{+4}_{-4}	45^{+15}_{-7}
^{44}S	0_1^+	0_2^+	2_1^+	2_2^+	4_1^+	4_2^+
E_x (MeV)	0.00	1.31	1.39	2.02	2.76	3.09
Q_s (e fm^2)	-	-	-6.0	4.7	15.5	-14.3
β	0.21(2)	0.21(1)	0.21(1)	0.21(2)	0.19(1)	0.20(1)
$\gamma(^\circ)$	31^{+7}_{-7}	25^{+6}_{-7}	26^{+7}_{-7}	30^{+8}_{-8}	24^{+5}_{-6}	14^{+5}_{-8}

In the $N = 28$ Mg, Si, and S isotopes, the low-lying structures differ not only in the magnitude of quadrupole collectivity, but also in their triaxiality indicators. Table 1 lists the detailed values of E_x, Q_s, β, and γ for ^{40}Mg, ^{42}Si, and ^{44}S. In ^{40}Mg, the 0_1^+, 2_1^+, and 4_1^+ states have similar large β values, small γ values, and negative Q_s values for the 2_1^+ and 4_1^+ states, supporting a coherent prolate band. In contrast, the 0_2^+, 2_2^+, and 4_2^+ states in

^{40}Mg have comparable β values and also prolate-side γ values, while the Q_s values of the 2_2^+ and 4_2^+ states are positive. The positive Q_s values of the 2_2^+ and 4_2^+ states indicate that the 0_2^+-associated structure is distinct from the ground-state band. However, the invariant-derived γ values of the 0_2^+, 2_2^+, and 4_2^+ states in ^{40}Mg lie in the prolate-side to triaxial region, showing that this structure should not be interpreted as a simple rigid oblate band. Similar β and γ values are observed for the 0_1^+, 2_1^+, and 4_1^+ states in ^{42}Si, but their γ values lie close to the oblate side and the corresponding Q_s values are positive.

For ^{44}S, the $E2$-transition pattern discussed below associates the 0_1^+, 2_1^+, and 4_2^+ states with a common quadrupole-connected sequence, in agreement with the SM calculations [30]. This assignment is consistent with the signs of the spectroscopic quadrupole moments, since $Q_s(2_1^+)$ and $Q_s(4_2^+)$ are both negative, whereas $Q_s(4_1^+)$ is positive. However, the γ value of the 4_2^+ state differs from those of the 0_1^+ and 2_1^+ states, indicating that this sequence is a band-like structure with non-rigid collectivity. Therefore, the β and γ values provide state-resolved deformation information, while the $E2$-transition maps are required to identify the quadrupole-connected structures directly.

Figure 3 displays the $E2$-transition maps for the $N = 27$, 28, and 29 Mg, Si, and S isotopes. The $E2$ connectivity clearly identifies the main band-like sequences. In ^{40}Mg and ^{42}Si, the strong $E2$ links among the 0_1^+, 2_1^+, and 4_1^+ states support their assignment to the ground-state band. In ^{44}S, however, the corresponding sequence is formed by the 0_1^+, 2_1^+, and 4_2^+ states, while the 4_1^+ state has weak downward $E2$ transitions and is interpreted as an isomeric bandhead, as discussed in Ref. [20]. Similarly, in ^{43}S and ^{45}S, the $7/2_1^-$ states can be regarded as candidate isomeric states, coexisting with the ground-state $3/2_1^-$ [21].

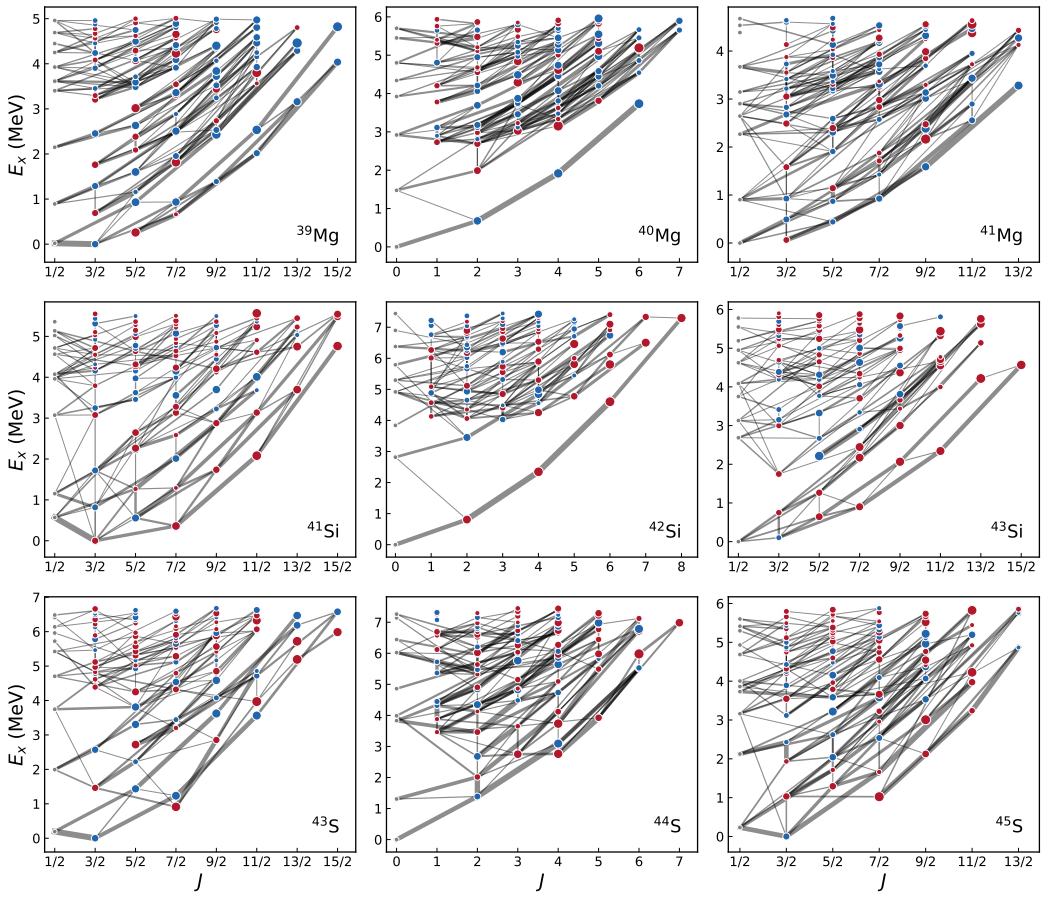

Figure 3. Calculated $E2$-transition maps for Mg, Si, and S isotopes around $N = 28$. The size of each dot indicates the magnitude of the Q_s and the color denotes its sign, with blue (red) corresponding to negative (positive) values. Line widths indicate downward $B(E2)$ strengths.

To show the shape evolution more clearly, Figure 4 presents the β-γ plane for the $N = 27$, 28, and 29 Mg, Si, and S isotopes. The low-lying states in the Mg isotopes are located around $\beta \approx 0.28$–0.31 and $\gamma \approx 10^\circ$–20°, indicating a common strong prolate deformation across the $N = 27$, 28, and 29 Mg systems. The Si isotopes show a markedly different pattern. The low-lying negative-parity states in ^{41,43}Si appear on the oblate side, and the 0_1^+, 2_1^+, and 4_1^+ states in ^{42}Si are also located near large γ values, around $\gamma \approx 55^\circ$. In contrast, the 0_2^+ and 2_2^+ states of ^{42}Si move to the smaller γ region, with a large fluctuation range, indicating a γ-soft structure. Furthermore, the low-lying states in ^{43,44,45}S mainly lie at $\beta \approx 0.18$–0.21 and $\gamma \approx 15^\circ$–30°, indicating prolate-side to triaxial deformation.

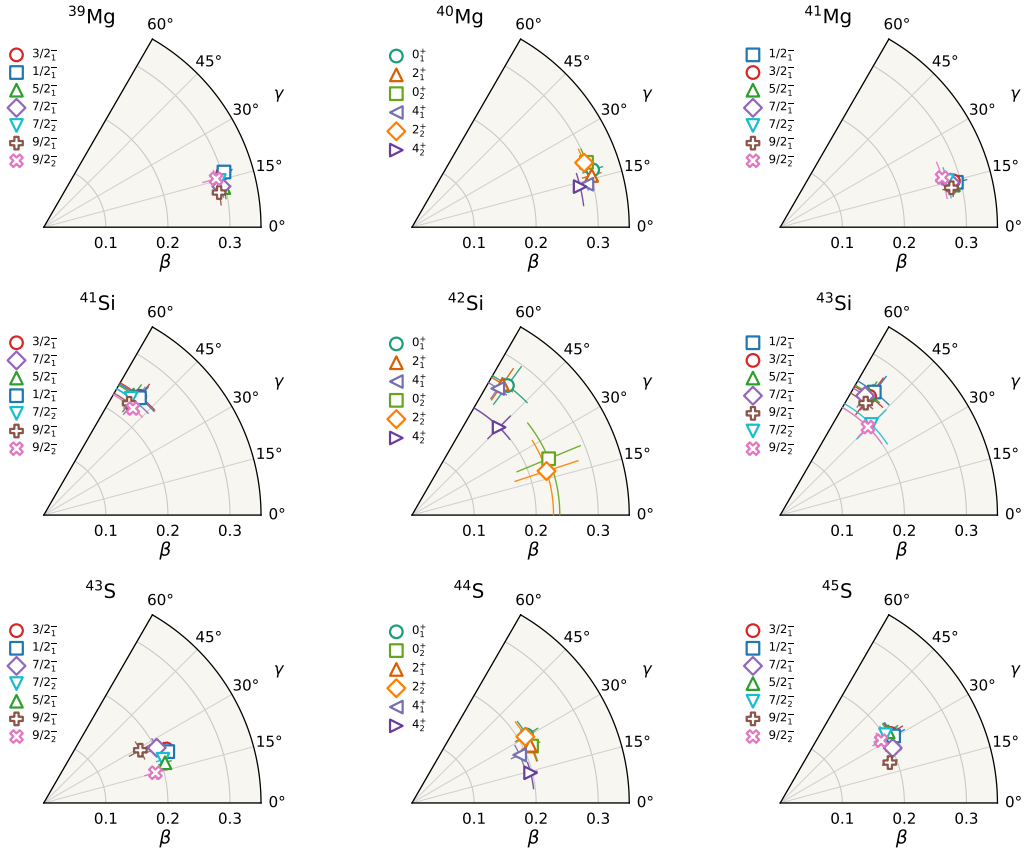

Figure 4. State-resolved β-γ fan plot for Mg, Si, and S isotopes. The radial coordinate denotes β and the angular coordinate denotes γ.

4. Conclusions

We have applied the quadrupole-invariant method to ab initio VS-IMSRG calculations of neutron-rich nuclei around $N = 28$. Starting from chiral NN+3N interactions, effective valence-space Hamiltonians and consistently evolved $E2$ operators are obtained and used to extract deformation parameters β and γ. Along the even–even $N = 28$ isotonic chain, the systematic increase of β from ^{48}Ca to ^{40}Mg provides a direct deformation signature of the weakening of the $N = 28$ shell closure and the growth of quadrupole collectivity. The extracted β and γ values further indicate a prolate–oblate–triaxial evolution of the 0_1^+ states from ^{40}Mg to ^{42}Si and ^{44}S. In contrast, the 0_2^+ states show comparable quadrupole collectivity but follow a different γ evolution, mainly lying in the prolate-to-triaxial region. In particular, the large γ-fluctuation range of the 0_2^+ state in ^{42}Si suggests a γ-soft structure. By combining the extracted β and γ values with Q_s systematics and the calculated $E2$-transition maps, we analyzed the state-by-state organization of the low-lying quadrupole structures. For ^{44}S, although the 0_1^+, 2_1^+, and 4_2^+ states form a quadrupole-connected

band-like sequence, the γ value of the 4_2^+ state differs from those of the 0_1^+ and 2_1^+ states, indicating non-rigid collectivity. Thus, the β and γ values provide state-resolved deformation information, while the $E2$-transition maps are needed to identify the quadrupole-connected structures directly. Extending the analysis to the neighboring $N = 27$ and $N = 29$ isotopes, we find a systematic shape evolution across the Mg, Si, and S chains: strong prolate deformation in Mg, oblate structures in Si, and prolate-to-triaxial deformation in S. These results demonstrate that quadrupole invariants built from ab initio $E2$ matrix elements offer a useful probe of shape evolution and shape coexistence in the neutron-rich $N \approx 28$ region.

Author Contributions: Conceptualization, L.-Y.S., X.-P.W., H.-H.L., H.-Y.Z., W.Z. and Q.Y.; methodology, L.-Y.S., X.-P.W. and Q.Y.; software, X.-P.W. and Q.Y.; validation, L.-Y.S., X.-P.W. and Q.Y.; formal analysis, L.-Y.S., X.-P.W., H.-H.L., H.-Y.Z., W.Z. and Q.Y.; investigation, L.-Y.S., X.-P.W., H.-H.L., H.-Y.Z., W.Z. and Q.Y.; resources, L.-Y.S. and Q.Y.; data curation, L.-Y.S. and Q.Y.; writing—original draft preparation, L.-Y.S. and Q.Y.; writing—review and editing, L.-Y.S. and Q.Y.; visualization, L.-Y.S. and Q.Y.; supervision, Q.Y.; project administration, Q.Y.; funding acquisition, W.Z. and Q.Y. All authors have read and agreed to the published version of the manuscript.

Funding: This work has been supported by the National Key R&D Program of China under Grant Nos. 2024YFE0109800, 2024YFE0109802, and 2023YFA1606403; the National Natural Science Foundation of China under Grant Nos. 12347106, 12405141, 12205340, 12175281, 12475128, 12322507, and 12121005.

Data Availability Statement: The original contributions presented in this study are included in the article. Further inquiries can be directed to the corresponding author.

Acknowledgments: We thank Takayuki Miyagi for the `NuHamil` code [73] used to generate matrix elements of the chiral three-body interaction, and Ragnar Stroberg for the `imsrg++` code [74] used to perform VS-IMSRG calculations. The numerical calculations in this work were performed at the Hefei Advanced Computing Center.

Conflicts of Interest: The authors declare no conflicts of interest.

Abbreviations

The following abbreviations are used in this manuscript:

SM	shell-model
BMF	beyond-mean-field
AMD	antisymmetrized molecular dynamics
VS-IMSRG	valence-space in-medium similarity renormalization group

References

1. Goeppert-Mayer, M. On Closed Shells in Nuclei. II. *Phys. Rev.* **1949**, *75*, 1969–1970. [CrossRef]
2. Haxel, O.; Jensen, J.H.D.; Suess, H.E. On the "Magic Numbers" in Nuclear Structure. *Phys. Rev.* **1949**, *75*, 1766. [CrossRef]
3. Warburton, E.K.; Becker, J.A.; Brown, B.A. Mass systematics for $A = 29$–44 nuclei: The deformed $A \sim 32$ region. *Phys. Rev. C* **1990**, *41*, 1147–1166. [CrossRef] [PubMed]
4. Sorlin, O.; Porquet, M.G. Nuclear magic numbers: New features far from stability. *Prog. Part. Nucl. Phys.* **2008**, *61*, 602–673. [CrossRef]
5. Caurier, E.; Martinez-Pinedo, G.; Nowacki, F.; Poves, A.; Zuker, A.P. The shell model as a unified view of nuclear structure. *Rev. Mod. Phys.* **2005**, *77*, 427–488. [CrossRef]
6. Otsuka, T.; Gade, A.; Sorlin, O.; Suzuki, T.; Utsuno, Y. Evolution of shell structure in exotic nuclei. *Rev. Mod. Phys.* **2020**, *92*, 015002. [CrossRef]
7. Tsunoda, N.; Otsuka, T.; Takayanagi, K.; Shimizu, N.; Suzuki, T.; Utsuno, Y.; Yoshida, S.; Ueno, H. The impact of nuclear shape on the emergence of the neutron dripline. *Nature* **2020**, *587*, 66–71. [CrossRef] [PubMed]
8. Shen, L.Y.; Yuan, Q.; Li, H.H.; Xie, M.R.; Li, J.G.; Zuo, W. Study of shell evolution in neutron-rich boron, carbon, and nitrogen isotopes with in-medium similarity renormalization group calculations. *Nucl. Sci. Tech.* **2025**, *36*, 220. [CrossRef]
9. Iwasaki, H.; Dewald, A.; Fransen, C.; Gelberg, A.; Hackstein, M.; Jolie, J.; Zell, K.O. Low-lying neutron intruder state in ^{13}B and the fading of the $N = 8$ shell closure. *Phys. Rev. Lett.* **2009**, *102*, 202502. [CrossRef] [PubMed]

10. Bastin, B.; Grévy, S.; Sohler, D.; Sorlin, O.; Dombrádi, Z.; Achouri, N.L.; Poves, A. Collapse of the $N = 28$ shell closure in ^{42}Si. *Phys. Rev. Lett.* **2007**, *99*, 022503. [CrossRef] [PubMed]
11. Force, C.; Grévy, S.; Gaudefroy, L.; Sorlin, O.; Cáceres, L.; Rotaru, F.; Nowacki, F. Prolate-spherical shape coexistence at $N = 28$ in ^{44}S. *Phys. Rev. Lett.* **2010**, *105*, 102501. [CrossRef] [PubMed]
12. Takeuchi, S.; Matsushita, M.; Aoi, N.; Doornenbal, P.; Li, K.; Motobayashi, T.; Yoneda, K. Well developed deformation in ^{42}Si. *Phys. Rev. Lett.* **2012**, *109*, 182501. [CrossRef] [PubMed]
13. Steppenbeck, D.; Takeuchi, S.; Aoi, N.; Doornenbal, P.; Matsushita, M.; Wang, H.; Yoneda, K. Evidence for a new nuclear 'magic number' from the level structure of ^{54}Ca. *Nature* **2013**, *502*, 207–211. [CrossRef] [PubMed]
14. Doornenbal, P.; Sheit, H. In-beam γ-ray spectroscopy of ^{34,36,38}Mg: Merging the $N = 20$ and $N = 28$ shell quenching. *Phys. Rev. Lett.* **2013**, *111*, 212502. [CrossRef] [PubMed]
15. Crawford, H.L.; Clark, R.M.; Fallon, P.; Macchiavelli, A.O.; Baugher, T.; Bazin, D.; Winkler, R. Quadrupole Collectivity in Neutron-Rich Fe and Cr Isotopes. *Phys. Rev. Lett.* **2013**, *110*, 242701. [CrossRef] [PubMed]
16. Crawford, H.L.; Fallon, P.; Macchiavélli, A.O.; Clark, R.M.; Brown, B.A.; Tostevin, J.A.; Yoneda, K. Shell and shape evolution at $N = 28$: The ^{40}Mg ground state. *Phys. Rev. C* **2014**, *89*, 041303(R). [CrossRef]
17. Gade, A.; Brown, B.A.; Tostevin, J.A.; Bazin, D.; Bender, P.C.; Campbell, C.M.; Weisshaar, D. Is the structure of ^{42}Si understood? *Phys. Rev. Lett.* **2019**, *122*, 222501. [CrossRef] [PubMed]
18. Crawford, H.L.; Fallon, P.; Macchiavelli, A.O.; Doornenbal, P.; Aoi, N.; Browne, F.; Wimmer, K. First spectroscopy of the near drip-line nucleus ^{40}Mg. *Phys. Rev. Lett.* **2019**, *122*, 052501. [CrossRef] [PubMed]
19. Longfellow, B.; Weisshaar, D.; Gade, A.; Brown, B.A.; Bazin, D.; Brown, K.W.; Spieker, M. Shape changes in the $N = 28$ island of inversion: Collective structures built on configuration-coexisting states in ^{43}S. *Phys. Rev. Lett.* **2020**, *125*, 232501. [CrossRef] [PubMed]
20. Yuan, Q.; Li, J.G.; Li, H.H. Ab initio calculations for well deformed nuclei: ^{40}Mg and ^{42}Si. *Phys. Lett. B* **2024**, *848*, 138331. [CrossRef]
21. Yuan, Q.; Li, J.G.; Zuo, W. Ab initio calculations for configuration-coexisting states in ^{45}S: An extension from ^{43}S. *Phys. Rev. C* **2024**, *109*, L041301. [CrossRef]
22. Caurier, E.; Nowacki, F.; Poves, A. The shell closure; from $N = Z$ to the neutron drip line. *Nucl. Phys. A* **2004**, *742*, 14–26. [CrossRef]
23. Nowacki, F.; Poves, A. New effective interaction for $0\hbar\omega$ shell-model calculations in the *sd-pf* valence space. *Phys. Rev. C* **2009**, *79*, 014310. [CrossRef]
24. Utsuno, Y.; Otsuka, T.; Brown, B.A.; Honma, M.; Mizusaki, T.; Shimizu, N. Shape transitions in exotic Si and S isotopes and tensor-force-driven Jahn-Teller effect. *Phys. Rev. C* **2012**, *86*, 051301(R). [CrossRef]
25. Utsuno, Y.; Shimizu, N.; Otsuka, T.; Yoshida, T.; Tsunoda, Y. Nature of Isomerism in Exotic Sulfur Isotopes. *Phys. Rev. Lett.* **2015**, *114*, 032501. [CrossRef] [PubMed]
26. Gaudefroy, L. Shell model study of $N \simeq 28$ neutron-rich nuclei. *Phys. Rev. C* **2010**, *81*, 064329. [CrossRef]
27. Kaneko, K.; Sun, Y.; Mizusaki, T.; Hasegawa, M. Shell-model study for neutron-rich *sd*-shell nuclei. *Phys. Rev. C* **2011**, *83*, 014320. [CrossRef]
28. Suzuki, Y.; Horiuchi, W.; Kimura, M. Erosion of $N = 28$ shell closure: Shape coexistence and monopole transition. *Prog. Theor. Exp. Phys.* **2022**, *2022*, 063D02. [CrossRef]
29. Caurier, E.; Nowacki, F.; Poves, A. Merging of the islands of inversion at $N = 20$ and $N = 28$. *Phys. Rev. C* **2014**, *90*, 014302. [CrossRef]
30. Chevrier, R.; Gaudefroy, L. Shell model structure of ^{43}S and ^{44}S re-examined. *Phys. Rev. C* **2014**, *89*, 051301(R). [CrossRef]
31. Tarpanov, D.; Liang, H.; Giai, N.V.; Stoyanov, C. Mean-field study of single-particle spectra evolution in $Z = 14$ and $N = 28$ chains. *Phys. Rev. C* **2008**, *77*, 054316. [CrossRef]
32. Rodríguez-Guzmán, R.; Egido, J.L.; Robledo, L.M. Quadrupole collectivity in $N \approx 28$ nuclei with the angular momentum projected generator coordinate method. *Phys. Rev. C* **2002**, *65*, 024304. [CrossRef]
33. Rodríguez, T.R.; Egido, J.L. Configuration mixing description of the nucleus ^{44}S. *Phys. Rev. C* **2011**, *84*, 051307(R). [CrossRef]
34. Egido, J.L.; Borrajo, M.; Rodríguez, T.R. Collective and Single-Particle Motion in Beyond Mean Field Approaches. *Phys. Rev. Lett.* **2016**, *116*, 052502. [CrossRef] [PubMed]
35. Kimura, M.; Taniguchi, Y.; Kanada-En'yo, Y.; Horiuchi, H.; Ikeda, K. Prolate, oblate, and triaxial shape coexistence, and the lost magicity of $N = 28$ in ^{43}S. *Phys. Rev. C* **2013**, *87*, 011301(R). [CrossRef]
36. Suzuki, Y.; Kimura, M. Triaxial deformation and the disappearance of the $N = 28$ shell gap. *Phys. Rev. C* **2021**, *104*, 024327. [CrossRef]
37. Yuan, Q.; Fan, S.Q.; Hu, B.S.; Li, J.G.; Zhang, S.; Wang, S.M.; Sun, Z.H.; Ma, Y.Z.; Xu, F.R. Deformed in-medium similarity renormalization group. *Phys. Rev. C* **2022**, *105*, L061303. [CrossRef]
38. Heyde, K.; Wood, J.L. Shape coexistence in atomic nuclei. *Rev. Mod. Phys.* **2011**, *83*, 1467–1521. [CrossRef]

39. Garrett, P.E.; Zielińska, M.; Clément, E. An experimental view on shape coexistence in nuclei. *Prog. Part. Nucl. Phys.* **2022**, *124*, 103931. [CrossRef]
40. Macchiavelli, A.O.; Crawford, H.L.; Campbell, C.M.; Clark, R.M.; Cromaz, M.; Fallon, P.; Rice, E. Structure of ^{43}P and ^{42}Si in a two-level shape-coexistence model. *Phys. Rev. C* **2022**, *105*, 014309. [CrossRef]
41. Sarazin, F.; Savajols, H.; Mittig, W.; Nowacki, F.; Orr, N.A.; Ren, Z.; De Vismes, A. Shape coexistence and the $N = 28$ shell closure far from stability. *Phys. Rev. Lett.* **2000**, *84*, 5062. [CrossRef] [PubMed]
42. Becheva, E.; Blumenfeld, Y.; Khan, E.; Beaumel, D.; Daugas, J.M.; Delaunay, F.; Than, H.S. $N = 14$ shell closure in ^{22}O viewed through a neutron sensitive probe. *Phys. Rev. Lett.* **2006**, *96*, 012501. [CrossRef] [PubMed]
43. Gaudefroy, L.; Sorlin, O.; Beaumel, D.; Blumenfeld, Y.; Dombrádi, Z.; Fortier, S.; Verney, D. Reduction of the spin-orbit splittings at the $N = 28$ shell closure. *Phys. Rev. Lett.* **2006**, *97*, 092501. [CrossRef] [PubMed]
44. Gaudefroy, L.; Daugas, J.M.; Hass, M.; Grévy, S.; Stodel, C.; Thomas, J.C.; Simpson, G. Shell erosion and shape coexistence in $^{43}_{16}S_{27}$. *Phys. Rev. Lett.* **2009**, *102*, 092501. [CrossRef] [PubMed]
45. Santiago-Gonzalez, D.; Wiedenhöver, I.; Abramkina, V.; Avila, M.L.; Baugher, T.; Bazin, D.; Weisshaar, D. Triple configuration coexistence in ^{44}S. *Phys. Rev. C* **2011**, *83*, 061305(R). [CrossRef]
46. Cáceres, L.; Sohler, D.; Grévy, S.; Sorlin, O.; Dombradi, Z.; Bastin, B.; Stefan, I. In-beam spectroscopic studies of the ^{44}S nucleus. *Phys. Rev. C* **2012**, *85*, 024311. [CrossRef]
47. Chevrier, R.; Daugas, J.M. Is the $7/2^-_1$ isomer state of ^{43}S spherical? *Phys. Rev. Lett.* **2012**, *108*, 162501. [CrossRef] [PubMed]
48. Parker, J.J.; Wiedenhöver, I.; Cottle, P.D.; Baker, J.; McPherson, D.; Riley, M.A.; Wimmer, K. Isomeric character of the lowest observed 4^+ state in ^{44}S. *Phys. Rev. Lett.* **2017**, *118*, 052501. [CrossRef] [PubMed]
49. Kumar, K. Intrinsic Quadrupole Moments and Shapes of Nuclear Ground States and Excited States. *Phys. Rev. Lett.* **1972**, *28*, 249–253. [CrossRef]
50. Srebrny, J.; Cline, D. Model independent determination of quadrupole deformation parameters from Coulomb excitation measurements. *Int. J. Mod. Phys. E* **2011**, *20*, 422–430. [CrossRef]
51. Hadyńska-Klęk, K.; Napiorkowski, P.J.; Zielińska, M.; Srebrny, J.; Maj, A. Quadrupole collectivity in ^{42}Ca from low-energy Coulomb excitation with AGATA. *Phys. Rev. C* **2018**, *97*, 024326. [CrossRef]
52. Henderson, J. Convergence of electric quadrupole rotational invariants from the nuclear shell model. *Phys. Rev. C* **2020**, *102*, 054306. [CrossRef]
53. Epelbaum, E.; Hammer, H.W.; Meißner, U.G. Modern theory of nuclear forces. *Rev. Mod. Phys.* **2009**, *81*, 1773–1825. [CrossRef]
54. Machleidt, R.; Entem, D.R. Chiral effective field theory and nuclear forces. *Phys. Rep.* **2011**, *503*, 1–75. [CrossRef]
55. Hebeler, K.; Bogner, S.K.; Furnstahl, R.J.; Nogga, A.; Schwenk, A. Improved nuclear matter calculations from chiral low-momentum interactions. *Phys. Rev. C* **2011**, *83*, 031301(R). [CrossRef]
56. Simonis, J.; Hebeler, K.; Holt, J.D.; Menendez, J.; Schwenk, A. Exploring sd-shell nuclei from two- and three-nucleon interactions with realistic saturation properties. *Phys. Rev. C* **2016**, *93*, 011302(R). [CrossRef]
57. Miyagi, T.; Stroberg, S.R.; Navrátil, P.; Hebeler, K.; Holt, J.D. Converged ab initio calculations of heavy nuclei. *Phys. Rev. C* **2022**, *105*, 014302. [CrossRef]
58. Roth, R.; Binder, S.; Vobig, K.; Calci, A.; Langhammer, J.; Navrátil, P. Medium-mass nuclei with normal-ordered chiral NN+3N interactions. *Phys. Rev. Lett.* **2012**, *109*, 052501. [CrossRef] [PubMed]
59. Morris, T.D.; Parzuchowski, N.M.; Bogner, S.K. Magnus expansion and in-medium similarity renormalization group. *Phys. Rev. C* **2015**, *92*, 034331. [CrossRef]
60. Tsukiyama, K.; Bogner, S.K.; Schwenk, A. In-medium similarity renormalization group for nuclei. *Phys. Rev. C* **2012**, *85*, 061304(R). [CrossRef]
61. Hergert, H.; Bogner, S.K.; Morris, T.D.; Schwenk, A.; Tsukiyama, K. The in-medium similarity renormalization group: A novel ab initio method for nuclei. *Phys. Rep.* **2016**, *621*, 165–222. [CrossRef]
62. Stroberg, S.R.; Calci, A.; Hergert, H.; Holt, J.D.; Bogner, S.K.; Roth, R.; Schwenk, A. Nucleus-dependent valence-space approach to nuclear structure. *Phys. Rev. Lett.* **2017**, *118*, 032502. [CrossRef] [PubMed]
63. Somà, V.; Navrátil, P.; Raimondi, F.; Barbieri, C.; Duguet, T. Novel chiral Hamiltonian and observables in light and medium-mass nuclei. *Phys. Rev. C* **2020**, *101*, 014318. [CrossRef]
64. Stroberg, S.R.; Holt, J.D.; Schwenk, A.; Simonis, J. Ab initio limits of atomic nuclei. *Phys. Rev. Lett.* **2021**, *126*, 022501. [CrossRef] [PubMed]
65. Shimizu, N.; Mizusaki, T.; Utsuno, Y.; Tsunoda, Y. Thick-restart block Lanczos method for large-scale shell-model calculations. *Comput. Phys. Commun.* **2019**, *244*, 372–384. [CrossRef]
66. Ring, P.; Schuck, P. *The Nuclear Many-Body Problem*; Springer: Berlin, Germany , 1980. [CrossRef]
67. Stroberg, S.R.; Henderson, J.; Hackman, G.; Ruotsalainen, P.; Hagen, G.; Holt, J.D. Systematics of $E2$ Strength in the *sd* Shell with the Valence-Space In-Medium Similarity Renormalization Group. *Phys. Rev. C* **2022**, *105*, 034333. [CrossRef]

68. Longfellow, B.; Weisshaar, D.; Gade, A.; Brown, B.A.; Bazin, D.; Brown, K.W.; Elman, B.; Pereira, J.; Rhodes, D.; Spieker, M. Quadrupole Collectivity in the Neutron-Rich Sulfur Isotopes ^{38,40,42,44}S. *Phys. Rev. C* **2021**, *103*, 054309. [CrossRef]
69. Elliott, J.P. Collective Motion in the Nuclear Shell Model. I. Classification Schemes for States of Mixed Configurations. *Proc. R. Soc. Lond. A* **1958**, *245*, 128–145. [CrossRef]
70. Elliott, J.P. Collective Motion in the Nuclear Shell Model. II. The Introduction of Intrinsic Wave-Functions. *Proc. R. Soc. Lond. A* **1958**, *245*, 562–581. [CrossRef]
71. Elliott, J.P.; Harvey, M. Collective Motion in the Nuclear Shell Model. III. The Calculation of Spectra. *Proc. R. Soc. Lond. A* **1963**, *272*, 557–577. [CrossRef]
72. Bonatsos, D.; Kota, V.K.B.; Martinou, A.; Peroulis, S.K.; Petrellis, D.; Vasileiou, P.; Mertzimekis, T.J.; Minkov, N. Parameter-Free Deformation Variables of the Proxy-SU(3) Symmetry in Even–Even Atomic Nuclei with $Z = 28$–82, $N = 28$–126. *Symmetry* **2026**, *18*, 683. [CrossRef]
73. Miyagi, T. NuHamil: A numerical code to generate nuclear two- and three-body matrix elements from chiral effective field theory. *Eur. Phys. J. A* **2023**, *59*, 150. [CrossRef] [PubMed]
74. Stroberg, S.R. Imsrg++ Code. Available online: https://github.com/ragnarstroberg/imsrg (accessed on 1 September 2019).

Disclaimer/Publisher's Note: The statements, opinions and data contained in all publications are solely those of the individual author(s) and contributor(s) and not of MDPI and/or the editor(s). MDPI and/or the editor(s) disclaim responsibility for any injury to people or property resulting from any ideas, methods, instructions or products referred to in the content.